Postprint of: Journal of Membrane Science 630 (2021) 119057
https://doi.org/10.1016/j.memsci.2021.119057
Submitted on 6th October 2020 / Revised 5th January 2021 / Accepted 5th Januarty 2021

High CO_2 permeability in supported molten-salt membranes with highly dense and aligned pores produced by directional solidification

L. Grima[1], G. A. Mutch[2], P. B. Oliete[1], W. Bucheli[1], R. I. Merino[1], E. I. Papaioannou[2], J. J. Bailey[3,4], M.D. Kok[3,4], D. J. L. Brett[3,4], P. R. Shearing[3,4], I. S. Metcalfe[2], M. L. Sanjuán[1,*]

[1]Instituto de Nanociencia y Materiales de Aragón (INMA), CSIC-Universidad de Zaragoza, Facultad de Ciencias, Universidad de Zaragoza, 50009 Zaragoza, Spain
[2]Materials, Concepts and Reaction Engineering (MatCoRE) Research Group, School of Engineering, Newcastle University, Newcastle-upon-Tyne, NE1 7RU, UK
[3]The Electrochemical Innovation Lab, Department of Chemical Engineering, University College London, London, WC1E 7JE, UK
[4]The Faraday Institution, Quad One, Becquerel Ave, Harwell Campus, Didcot, OX11 0RA, UK.

Abstract

Composite molten salt-ceramic membranes are promising devices for high-temperature CO_2 separation. Intensive material properties impact on separation performance as do membrane geometry (thickness) and microstructure (pore volume fraction, size, connectivity, and tortuosity factor). Although controlling pore size is considered somewhat routine, achieving pore alignment and connectivity is still challenging. Here we report the production of the first gas separation membrane using a porous ceramic matrix obtained from a directionally-solidified magnesium-stabilised zirconia (MgSZ) – MgO fibrilar eutectic as the membrane support. MgO was removed from the parent material by acid-etching to create a porous matrix with highly aligned pores with diameters of ~1 µm. X-ray nano-computed tomography of a central portion (~32,000 μm^3) of the support identified ~21% porosity, with all pores aligned within 10° and ~76% percolating along the longest sampled length. Employing the matrix as a support for a carbonate molten salt, a high CO_2 permeability of 1.41×10^{-10} $mol.m^{-1}.s^{-1}.Pa^{-1}$ at 815 °C was achieved, among the highest reported for supported molten-carbonate membranes (typically 10^{-12} to 10^{-10} $mol.m^{-1}.s^{-1}.Pa^{-1}$ at similar temperatures). We suggest that the high permeability is attributable to the excellent pore characteristics resulting from directional solidification, namely a dense array of parallel, micron-scale pores connecting the feed and permeate sides of the membrane.

Keywords

CO_2 separation membranes; Dual-phase membranes; Permeation; MgSZ-MgO eutectic; Directional solidification

1. Introduction

High-performance membranes have short transport pathways of low tortuosity. If such a structure can be achieved, high-permeability membranes may provide transformative solutions for energy-intensive separations such as CO_2 capture. Supported molten-salt membranes are emerging as promising candidates for CO_2 separation due to their unrivalled and desirable combination of high selectivity and high permeability [1]. Furthermore, they are operable at the high-temperature conditions found in important applications including enhanced water-gas-shift or flue gas separation. Typically, they are composed of molten carbonate salts supported in the pore space of an inorganic solid [2,3]. Supports have included oxygen-ion and/or electron-conducting porous inorganic solids, however, to date their pore structures have been typically tortuous and unrefined. To further improve separation performance, promising intensive material properties (*e.g.* high ionic conductivity in the molten salt) should be paired with a membrane structure likely to provide high performance.

A conventional understanding of supported molten-salt membranes [4- 9] tells us that CO_2 permeation starts with the formation of CO_3^{2-} anions at the feed-side membrane surface, where gas, melt and solid support meet. The precise surface reactions depend on the nature of the support; for a purely ionic oxygen conductor it is postulated that CO_2 in the feed gas reacts with oxide ions from the ceramic support to form CO_3^{2-} ions that diffuse through the molten carbonate phase (Equation 1).

$$CO_{2\,(g)} + O^{2-}{}_{(s)} \rightleftarrows CO_3^{2-}{}_{(l)} \qquad (1)$$

Within this approach the permeate flux is given by Equation 2 [4,5,9]

$$J_{\mathrm{CO_2}} = \frac{RT}{4LF^2}\sigma_{eff}\, ln\left(\frac{p_{\mathrm{CO_2}}(\mathrm{permeate})}{p_{\mathrm{CO_2}}(\mathrm{feed})}\right), \qquad (2)$$

where L is the membrane thickness, p_{CO2}(feed) and p_{CO2}(permeate) are the CO_2 partial pressures at the feed and permeate sides, respectively, and σ_{eff} is the effective ambipolar conductivity that results from the simultaneous but separate transport of ionic species in the molten carbonate and solid oxide phases. Assuming a negligible electronic transport number in the support, the effective ambipolar conductivity is given by Equation 3.

$$\sigma_{\mathrm{eff}} = \frac{[(\varphi/\tau)_{\mathrm{c}}\sigma_{\mathrm{c}}][(\varphi/\tau)_{\mathrm{so}}\sigma_{\mathrm{so}}]}{[(\varphi/\tau)_{\mathrm{c}}\sigma_{\mathrm{c}}]+[(\varphi/\tau)_{\mathrm{so}}\sigma_{\mathrm{so}}]}, \qquad (3)$$

where σ_c, $(\varphi/\tau)_c$ and σ_{so}, $(\varphi/\tau)_{so}$ are the conductivity and volume-fraction-to-tortuosity-factor ratio of carbonate and solid oxide phases, respectively [9]. In the case of complete pore filling by carbonates, φ_c equals the support porosity, usually denoted by ε.

According to Equations 2 and 3, membrane performance depends on intensive material properties, such as molten carbonate and solid oxide conductivities, and on geometric and microstructural characteristics, with the latter influenced by the support preparation method. Laboratory-scale investigations have mainly focussed on membranes with supports prepared by isostatic pressing or tape-casting, due to the simplicity of preparation [4,10]. More recently, tubular supports have been investigated in an effort to move closer to membranes with an inherent affinity to scale-up [11-14]. However, in most cases, porosity control in the support relies upon the use of sacrificial materials, such as pore formers, where the quantity, size and shape of the pore former dictates the final porosity and pore structure of the support.

Although the model based on Equations 1 to 3 does not contain a full description of how the components of pore structure (pore volume, size, connectivity and tortuosity factor) impact on gas permeation, a relationship between permeation and properties, such as support particle interconnectivity, molten salt-support interfacial area, molten salt-gas interfacial area and total membrane conductivity, can be anticipated [9,2,3]. In a samarium-doped ceria (SDC)-carbonate system, for instance, the conductivity increased linearly with the SDC-carbonate interfacial area but was inversely proportional to the tortuosity factor [15]. In a lanthanum strontium cobalt ferrite (LSCF)-carbonate system, permeability could be increased (assuming the conductivity of the carbonate and oxygen-ion conducting support is fixed) by increasing the porosity-to-tortuosity-factor ratio (for the carbonate phase) and solid-fraction-to-tortuosity-factor ratio (for the ceramic phase) [9]. In an SDC-supported membrane, in which pore formers were employed to fabricate a highly-interconnected structure, a permeability above 10^{-10} $mol.m^{-1}.s^{-1}.Pa^{-1}$ was reported, suggesting that pore connectivity is important in achieving high permeability [16]. Recently, it was shown (using a nominally inert membrane support), that permeation rate is limited by molten salt-gas interfacial area at the permeate side [17], indicating that other mechanisms beyond Equation 1 at the triple-phase boundary (TPB) are involved, probably based on different interfacial reactions [3]. Taken together, it is clear that there is a need for support preparation methods that allow exquisite control of e.g. interfacial area, triple-phase boundary, and tortuosity factor in order to go beyond the conventional understanding of Equations 1 to 3 which struggle to explain much of the observed membrane behaviour.

Although progress has been made in achieving pore-size control [18-21], and in fabricating thin membranes [11,12,22], in general these methods lack directional control, *i.e.* the alignment of the pore structure with the direction of desired gas transport. Methods that generate ceramics with aligned porosity include freeze casting, impregnation with a ceramic slurry of an aligned sacrificial template, phase inversion and co-extrusion of ceramic and sacrificial pore-former [23-26]. Recently, micro-fabrication was used to produce supported molten-salt membranes with pores of ~10^2 µm diameter aligned with the direction of desired gas transport (by laser-drilling arrays of parallel pores into the closed end of a ceramic tube). In one example where the self-assembly of electronically-conductive Ag dendrites within the parallel pores was stimulated by gas permeation, an exceptionally high CO_2 flux (~1.25 $ml.min^{-1}.cm^{-2}$ at 650 °C) was achieved [27]. By comparison with a membrane having a sinuous pore network in the same work, the directionally-aligned pores were considered to be advantageous for performance. However, it is very challenging to generate dense arrays of micron-scale pores in ceramics with 3D micro-fabrication techniques, due to *e.g.* the limited spatial resolution of additive manufacturing or laser-drilling approaches. Directional-solidification methods provide an alternative means to prepare ceramics with aligned microstructures (*viz.* certain families of eutectics), giving rise to samples with 1 to 10^4 mm^2 cross-section areas and characteristic phase sizes from 0.1 to 10 µm in a direction transverse to the growth axis [28,29]. In the case of fibrilar eutectics, the technique provides a quasi-hexagonal array of highly aligned fibres of the minority phase, parallel to the growth direction, embedded into a single crystal of the majority phase. In principle, such a structure provides pores with a nominal tortuosity of unity (after removal of the fibre phase). Additionally, the structure should also afford a high interfacial area between the support and the molten salt, which may be important depending on the permeation mechanism.

The quality of the alignment, and the finesse and homogeneity of the microstructure afforded by directional solidification of eutectics far surpass what is observed in membranes produced by other pore-aligning methods, such as freeze-casting or phase-inversion. In hollow fibres produced by phase inversion, for instance, a bimodal radial distribution of pore size is usually found, with finger-like pores in a relatively large diameter range (≥4 µm, up to several tens) presenting a quite irregular shape and small pores (diameter below 1 µm) forming sponge-like regions [25,14].

Thus, here we show how fibrilar eutectics can be used to produce a molten-salt membrane support with geometrical and microstructural properties difficult to achieve by other methods. We employed the laser floating zone (LFZ) technique of directional solidification [29], through

which the high-melting-point oxides employed in supported molten-salt membranes may be melted and solidified with no need of a crucible, yielding mechanically strong, rod-shaped eutectic bi-crystals with no porosity. The minority phase (fibres) was removed by acid etching to produce a matrix with a highly dense array of aligned pores on a length scale difficult to achieve by other methods (<10^1 μm). The porous matrix was then employed as a support for molten carbonate infiltration; CO_2 permeation experiments provided an exceptionally high CO_2 permeability above 700 °C, a result that can be attributed to the optimisation of the pore microstructural properties, namely low tortuosity factor, high pore density and high specific interfacial area.

2. The ZrO_2-MgO phase diagram and materials properties

The desirable characteristics of a membrane support impose restrictive conditions on materials selection for directional solidification. First, fibrilar eutectic growth requires that the proportion of the minority phase does not exceed ~29 vol% [29]. Otherwise, lamellar growth will in general occur. Second, coupled growth must take place in order to achieve an ordered, colony-free, microstructure. Third, the minor phase (fibres) must be easily etched without affecting the matrix that will become the membrane support and said matrix should be an oxygen-ion conductor. Finally, thermal expansion compatibility is required between the materials forming the matrix and the fibres, to *e.g.* avoid cracks on cooling during solidification.

After exploring different systems, we found the ZrO_2-MgO system to be a suitable combination of oxides as it fulfils the requirements listed above. According to the ZrO_2-MgO phase diagram (PD) (Figure S1, ESI) [30], a eutectic point exists around 50:50 mol% ZrO_2:MgO with $T_e \approx 2170$ °C. A more precise determination of the eutectic composition yielded 47:53 mol% ZrO_2:MgO [31]. At the eutectic temperature, the liquid crystallizes in the form of a quasi-hexagonal lattice of micron-sized MgO fibres embedded within a magnesium-stabilised zirconia (MgSZ) cubic phase with ~20% Mg^{2+} content [31,32]. The incorporation of Mg^{2+} ions within the initially monoclinic ZrO_2 phase introduces a corresponding number of oxygen vacancies that stabilise MgSZ in its cubic form and provide ion-conducting behaviour. The volume proportion of the MgO fibres in the eutectic predicted by the PD is 28.7%, close to the limit between fibrilar and lamellar growth. The linear thermal expansion coefficients (TEC) of MgO and MgSZ match relatively well: the TEC of MgO varies from 11 to 14 x 10^{-6} K^{-1} between 300 and 1000 K [33], which is close to the TEC of cubic zirconia-related materials, 10.5-11 x 10^{-6} K^{-1} for YSZ (8 mol% Y_2O_3 doped ZrO_2) in the same temperature range and of the order of 11.2 x 10^{-6} K^{-1} for (3 mol% YSZ)$_{0.8}$-MgO$_{0.2}$ [34].

Directionally solidified MgO-MgSZ also shows suitable flexural strength, with values ranging from 150 to 450 MPa [35,36]. This hints towards the possibility of safely producing crack-free bicrystals during cooling after laser-assisted solidification. Moreover, although lower than YSZ ($\sigma \gtrsim 10^{-2}$ S.cm^{-1} at 1020 K) [37], which is routinely employed in supported molten-salt membranes, MgSZ still has a good ionic conductivity of 2.3 x 10^{-3} S.cm^{-1} at 1000 K [38]. Finally, MgO is highly soluble in hydrochloric acid whereas MgSZ is not, so that the fibres can be eliminated by acid-etching without significantly affecting the matrix.

Other material combinations might be suitable, provided that they fulfil the requirements listed above. Preliminary work is being carried out with the YSZ-MgO and $Zr_{1-x}Ce_xO_2$-MgO eutectics, although in the latter case, thermo-mechanical stability may be an issue.

3. Materials and methods

Rods of 47:53 mol% ZrO_2:MgO were directionally solidified using the LFZ method, where a drop of a sample is melted by focussing a high-power CO_2 laser on a small volume of the feedstock material as it moves vertically [29]. To prepare the feedstock rods, commercial powders of ZrO_2 (Aldrich, 99%) and MgO (Alfa Aesar, 99.99%) were mixed in the appropriate amount, isostatically pressed for 3 min at 200 MPa and sintered at 1500 °C for 12 h in an open furnace. Rods of ~80 mm length were melted and solidified in air using 80-100 W of a CO_2 laser (λ = 10.6 μm) as a heating source at rates varying between 10 and 300 mm.h^{-1}. The final diameters of the rods were between 1.2 and 1.5 mm.

Transverse and longitudinal cross-sections of the processed rods were cut and polished for scanning electron microscopy (SEM) and electron dispersive X-ray spectroscopy (EDS) in a Field Emission SEM microscope (MERLIN, Carl Zeiss). The volumetric phase proportion of the fibres and the matrix in the eutectics was calculated by greyscale analysis of transverse-section micrographs, performed by means of Digital Micrograph, Gatan Inc. software.

Crushed portions of the rods were used for X-ray diffraction (XRD) experiments, which were carried out on a Rigaku D/max 2500 diffractometer with Cu K_α radiation working at 40 kV and 100 mA. Data were collected in a step mode ($\Delta 2\theta$ = 0.03°) and a counting time of 3 s per step.

Sections of the rods were acid-etched by immersion in a 1 M solution of HCl in distilled water at 60 °C. The sample weight was measured to check the degree of etching, which was determined from the weight loss relative to the weight proportion (21%) of the MgO fibres in the MgSZ-MgO

eutectic. Achieving mass losses above 80% of the MgO phase required treatments lasting ≥20 days.

An as-etched eutectic sample was prepared for X-ray nano-CT by use of an A Series/Compact Laser Micromachining System (Oxford Lasers) with an embedded Class 4 laser with 532 nm wavelength. A small eutectic sample (~1.5 mm dimensions) was epoxy-glued to the end of a stainless-steel dowel which was laser-lathed to a fine cylinder with a diameter of approximately 40-50 µm. This procedure is detailed in [39].

X-ray nano CT was performed using a Zeiss Xradia 810 Ultra (Carl Zeiss), which has a micro-focus rotating Cr anode set at 35 kV and 25 mA. A pseudo-parallel X-ray beam was quasi-monochromatized at Cr K_α (5.4 keV) by a reflective capillary condenser, before impinging on the sample and subsequently being re-focused by a Fresnel zone plate onto a CCD detector. Scans were performed in absorption-contrast mode with a field-of-view of 65 × 65 µm, operated with a binning of 2, yielding a voxel dimension of ~126 nm. X-ray nano-CT projections were taken from -90 to +90° at 1101 regular angular increments, each with an exposure time of 64 s, the resultant projections of which were reconstructed in XMReconstructor (Carl Zeiss) using a traditional filtered back-projection algorithm.

The X-ray tomogram was imported into Avizo (Thermo Fisher Scientific) and first underwent a transform to align the pore direction with the *z*-direction of the tomogram. Subsequently, this transformed volume underwent a shading correction to compensate for grayscale gradients across the entire 3D volume. A sub-sample was removed from within this corrected, transformed volume with dimensions of ~25.2 × 25.2 × 50.5 µm, giving an overall sampled volume of ~32,100 μm^3. The sub-volume underwent a second shading correction before an Unsharp Masking filter (3D, edge size 5 pixels and edge contrast set to 0.5) and a Gaussian filter (3D, kernel size 5 pixels and standard deviation set to 1) was applied, to better highlight the pore-solid boundaries. The resultant sub-volume was then segmented using machine-learning-based freeware, Ilastik [40], with user training provided on one central slice. Subsequently, user interaction with several other slices was used to give an updated binary segmentation that was deemed to match the processed volume well by eye. Note that the MgO and MgSZ phases were not distinguishable at 5.4 keV and at this pillar width, such that the binary segmentation represents a delineation between porosity and a composite phase made up of both residual MgO and the MgSZ matrix.

Volume calculations for the two phases were made using simple voxel counting from the binarised dataset. All surface areas were calculated by generating a surface mesh (constrained

smoothing) and summing the areas of the resulting mesh elements. Volume-specific surface areas were calculated by dividing by the pore volume in question. This analysis was carried out for the entire dataset, as well as for datasets including only the isolated, non-isolated, *x*-connected, *y*-connected and *z*-connected porous components. The isolated (and thus by subtraction, non-isolated) components were accessed by a simple 3D 'Border Kill' algorithm which removed all objects that had an interface with the external boundary. The *x*-, *y*- and *z*-components of the porous phase were accessed using the 'Axis Connectivity' module in the *x*-, *y*- and *z*-directions, respectively.

To assess the pore parallelism, linear regression was performed in Python. To separate any adjoined pores, two successive binary opening processes were performed. Binary opening consists of an erosion step (removal of outermost pixels), followed by a dilation step (the converse process). The purpose was to maintain quite closely the shape of the original structures, but also to break any small connections between larger bodies. Due to either small irregularities in the segmentation, or small connections in the true structure, individual fibrils may begin this process with several small connections between them, making them appear numerically as one feature. After binary opening the large structures should no longer be connected. Indeed, after two successive operations, 140 separate pores were identified. Before regression, each pore was made smaller with two more erosions. As before, this maintained the shape but reduced the overall size of the data set. Two linear regressions were performed on each pore, one for the *x*-component versus the *z*-component and the other for the *y*-component versus the *z*-component.

The total electrical conductivity of the samples was calculated from resistance measured by impedance spectroscopy (SI 126.0 Schlumberger Instruments). The spectra were recorded by exciting the samples with amplitude voltages of 100 or 50 mV, from 1 to 10^6 Hz and sampling 10 frequency points per decade. Nyquist plots were used to extract the total resistance of the respective samples, excluding the electrode contribution [41]. For the MgSZ-MgO eutectic samples, the electrodes were made with Pt paste and cured at 900 °C for 0.5 h. The conductivity of the carbonate mixture was measured in a small Al_2O_3 crucible (capacity ~3 mm^3) with Pt sheets as electrodes. The Al_2O_3 crucible was filled with the carbonate mixture, heated above the eutectic temperature to eliminate bubbles in the mixture and then cooled to room temperature with the Pt-sheet electrodes in place. For the MgSZ samples infiltrated with carbonates, Au-paste electrodes were painted and cured at a temperature below the melting temperature of the carbonates. Infiltration of the carbonates into the porous MgSZ for conductivity measurements was made in ambient air. For that purpose, a mixture of Li_2CO_3, Na_2CO_3 and K_2CO_3

carbonates in the ternary eutectic proportion (42.5/32.5/25 mol%, respectively) was deposited in compacted powder form on top of the MgSZ sample and heated above the eutectic temperature (397 °C) to allow the carbonates to melt and infiltrate the pores by capillarity. All prepared samples were held against spring-loaded Pt sheets welded to Pt wires with the entire arrangement located in a cylindrical furnace for measurements. All measurements were made in stagnant air with temperature monitored with a K-type thermocouple located near the sample.

Supports for permeation experiments were infiltrated with the ternary eutectic mixture of alkaline carbonates following a similar procedure as for conductivity measurements. High-temperature carbon dioxide permeation experiments were carried out in a custom-made membrane reactor, operated at atmospheric pressure. The permeation apparatus comprises two chambers, an internal feed-side chamber and an external permeate-side chamber, enclosed by the membrane and a quartz tube, respectively. The details can be found elsewhere [42]. For an accurate temperature determination, a thermocouple was placed as close as possible to the membrane, with the membranes pasted to a YSZ tube using Au paste. The feed gas was 50 mol% CO_2/25 mol% N_2/25 mol% O_2 (feed-side inlet) and the sweep gas was high-purity Ar (permeate-side inlet). Different inert gases (N_2 on the feed side and Ar on the permeate side) were used to detect transmembrane leaks, *i.e.* if N_2 was detected significantly above background levels the experiments were stopped as a leak was apparent. All gases were provided and certified by BOC. The flows on both the feed and permeate sides were maintained at a total gas flow rate of 30 ml.min^{-1} (NTP). Residence time distribution experiments (not shown) for both the feed- and permeate-side chambers indicated that the membrane was exposed to the outlet conditions as there was good gas mixing on both sides. The outlet permeate-side gases (*e.g.* CO_2, N_2 or O_2) were analysed using a mass spectrometer (HIDEN, HALO 100-RC). The superposition of the CO and N_2 signals in the m/z= 28 channel was accounted for and the N_2 flow was corrected accordingly. The CO_2 concentration in the permeate-side outlet stream was also analysed using IR (XTREAM-Enhanced General-Purpose Process Gas (XEGP) Analyser, Emerson Process Management Limited) in series with and after the mass spectrometer. Both the IR analyser and the mass spectrometer were calibrated before each experiment to account for systematic errors and instrument drift, by flowing N_2 and CO_2 gases of certified mole fraction. The mole fraction of the calibration gases was chosen to be as close as possible to the expected permeate-side mole fraction during the permeation experiments. Argon was used for background calibration for all instruments. The flow of gases to the permeation apparatus was controlled by mass flow controllers (Brooks Smart II). Flow rates were confirmed at the permeate-side outlet using a

Varian digital flow meter (1000 series). From the measured permeation rate y (ml.min^{-1}) of each gas, the flux J (ml.min^{-1}.cm^{-2}) is defined as $J = y/A$, where A is the membrane area.

Raman spectroscopy of the matrix before and after etching as well as after permeation experiments (as a molten carbonate support) was performed in a DILOR XY spectrometer equipped with a liquid-nitrogen cooled CCD detector. The 496.5 nm line of an Ar^+-ion laser, model Coherent Innova 305, was used as excitation source. A 50X microscope objective lens of an Olympus BH-2 microscope was used both for excitation and dispersed light collection. The same microscope was used to record optical images of the samples.

4. Microstructure and conductivity of the supporting oxide

MgSZ-MgO eutectic rods were directionally solidified at different processing rates to test the influence of the solidification rate on phase microstructure. Rates above 50 mm.h^{-1} resulted in colony-like microstructures (Figure S2, ESI), such that we limited our study to 25 mm.h^{-1} processing rates (Figure 1).

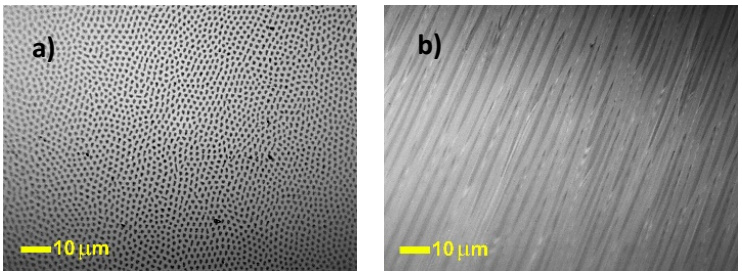

Figure 1. Optical micrographs of the: **a)** transverse and **b)** longitudinal sections of an MgSZ-MgO eutectic rod processed at 25 mm.h^{-1}. In this context, transverse and longitudinal mean perpendicular to, and containing the growth axis, respectively. The latter coincides with the fibre direction.

The as-grown rods consist of a quasi-hexagonal eutectic pattern of MgO fibres embedded in an MgSZ matrix (EDS analysis confirmed the fibres are 100% MgO whereas the composition of the matrix suggests that it is an MgSZ phase (Figure S3, ESI)). The fibre spacing λ of fibrilar eutectics depends on the growth rate v as per the Hunt-Jackson law $\lambda^2 v = C$ [43], where C is a constant for each system, which depends essentially on the phase diagram and the diffusion coefficient of the ions in the melt. For the MgSZ-MgO system with v = 25 mm h^{-1}, the fibre diameter was ~1 µm and the spacing was ~2 µm [32,36]. The phase proportion was determined from image analysis to be 29±1 vol% of MgO phase, in good agreement with the PD. The volume percentage of the fibre phase determines the maximum porosity of the matrix after etching, the actual porosity

being diminished with respect to the maximum value by the degree of unsuccessful etching. In our case, MgO weight losses between 80 and 90% were achieved, resulting in a support porosity in the 22.4 to 27% range. A digital image of the transverse section of a rod after etching is shown in Figure 2, confirming a tightly packed array of fine diameter (~1-1.5 µm) pores.

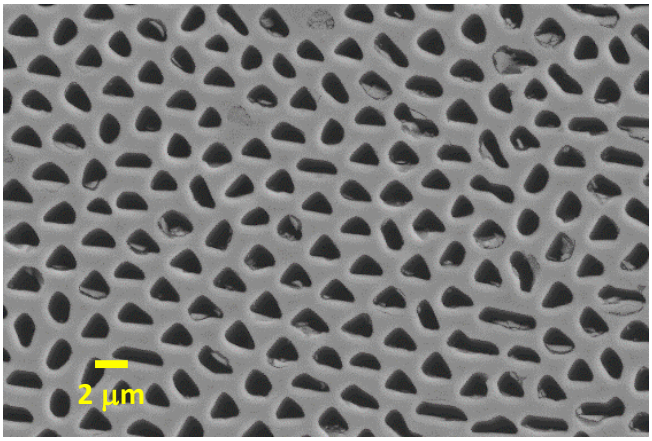

Figure 2. Electron micrograph of the transverse section (perpendicular to the growth axis) of an MgSZ-MgO eutectic solidified at 25 mm.h^{-1} after etching, depicting an array of micrometric pores (dark grayscale) embedded into the MgSZ matrix (light grayscale). Note that some of the fibres are occluded by polishing material due to polishing after etching.

To avoid the influence of nearby MgO fibres in the determination of the matrix composition, EDS analyses were also performed in etched samples and yielded a Mg cation content of about 16-17% in the matrix, which is below the prediction from the PD (~20%) (Figure S3, ESI). This difference can be attributed to the prolonged acid treatment of 2-3 weeks, an effect also observed by Sato *et al*. in bulk MgSZ samples [44]. Crushed portions of the samples were also analysed by XRD (no attempt was made to analyse the phase composition, as preferential orientation is expected in crushed single-crystals). XRD patterns were fitted with two phases (Figure S4, ESI), a fluorite phase belonging to the MgSZ matrix, with *a*(MgSZ) = 5.058(1) Å, and a rock-salt phase, accounting for the MgO fibres, with *a*(MgO) = 4.213(1) Å. Both values agree, within error, with those reported in the literature for this system and with the matrix composition determined by EDS [45].

4.1. X-ray nano-CT of the porous matrix

As the MgSZ matrices obtained by etching the MgSZ-MgO eutectics are to be used as supports for molten carbonate, the 3D microstructure of the matrices was studied by X-ray nano-CT to characterise the porosity in terms of phase fraction, isolation, connectivity and alignment.

Figure 3 shows 3D reconstructions of the X-ray nano-CT data from the thinned pillar of an etched rod, depicting the solid phase (Figure 3a) and the pores of the matrix (Figure 3b) prior to carbonate infiltration. In Figure 3c, 'families' of interconnected pores are shown, with 'families' uniquely coloured.

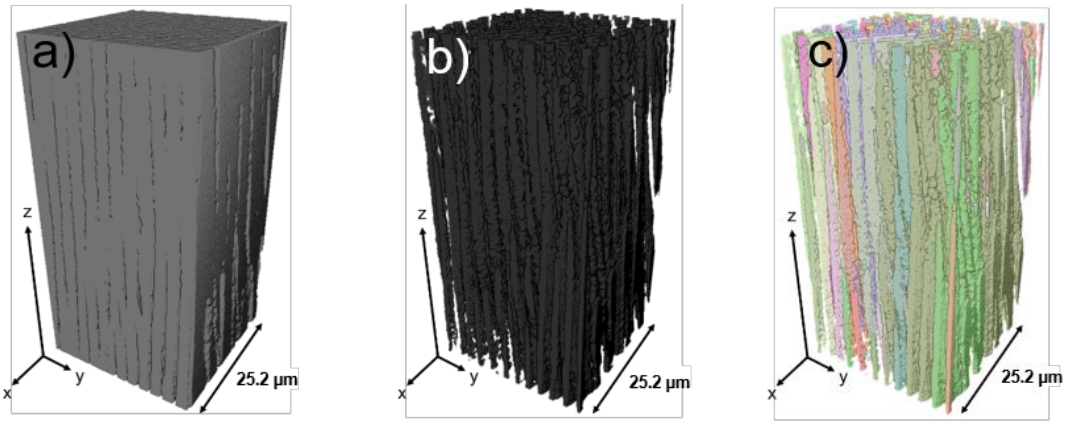

Figure 3. X-ray nano-CT volume renderings of the sample prior to carbonate infiltration. **a)** Image of solids, in which porosity in the MgSZ matrix is transparent. **b)** Image of all pores, in which the solids are removed, and the alignment of pores can be clearly observed; **c)** Image of individual pore 'families' (pores that have coalesced) uniquely coloured.

Table 1 shows the analysis of the full set of pores, the closed and open pores, and the pores percolating between each set of opposite faces (*x*-, *y*- and *z*-direction). A porosity of ~20.7% was identified from the entire analysed volume (~32,100 μm^3), with a volume-specific internal surface area of ~0.9 μm^{-1} (~0.8 μm^{-1} for *z*-percolating pores). The 20.7% porosity is slightly below the range determined from weight loss after acid treatment in these samples (22.4 - 27%), a discrepancy that can be attributed to the different nature of the techniques used for each determination. Weight loss is a macroscopic measurement that averages composition or microstructural inhomogeneity across the sample, whereas X-ray nano-CT gives the porosity of a small sample volume and depends on the segmentation used to define the limit between pore and solid phases. Most of the pores were connected to at least one plane of the analysed volume, leaving a negligible proportion of closed pores (0.24% of entire volume), consistent with the etching procedure. Although no pores percolated in the '*x*-direction', just over a third percolated in the '*y*-direction' and importantly for our aims, ~76% percolated in the '*z*-direction' (growth direction), across the ~50 µm section of the etched sample.

Table 1. Extracted metrics from X-ray nano-CT tomogram of thin MgSZ pillar of ~ 32,100 μm^3 total volume.

Porosity type	Absolute pore Volume (μm^3)	Fraction of total volume	Fraction of pore volume	Absolute Surface Area (μm^2)	Volume-specific Surface Area (μm^{-1})
All	6662	20.7%	100.0%	31356	4.7
Closed	76	0.2%	1.1%	632	8.3
Open	6586	20.5%	98.9%	30722	4.7
x-percolating	0	0%	0%	0	0
y-percolating	2467	7.7%	37.0%	11104	4.5
z-percolating	5077	15.8%	76.2%	23706	4.7

As can be seen in Figure 3c, most of the pores in the analysed volume are isolated from each other, a majority of them percolated between the top and bottom faces of the analysed volume. However, it can also be seen that there are some 'families' of connected pores, which arise from fibre coalescence in a transverse direction. This is not unusual in fibrilar eutectics; pores with irregular shape in a transverse direction can be seen in the electron micrographs depicted in Figure 2, although in that case only occasional fibre coalescence can be observed.

The results of the pore alignment calculations can be seen in Figure 4. As can be clearly seen, the fact that both the *x* and *y*- components of all the fibrils are very internally similar for each pore is testament to their parallelism. The small degree of scatter is a representation of their minor deviations from being fully parallel with one another, which constitutes a variation between -9.9 and 0.2 degrees, and -5.1 and 4.7 degrees, in the *x*- and *y*-direction, respectively. The fact that the scatter is not centred about zero in the *x*-direction is simply an artefact of the initial, imperfect transformation used to align the pores to the *z*-direction. Since the range of deviations is 9.7 and 9.8 degrees, in the *x*- and *y*-direction, respectively, there is no evidence of anisotropy in the measured deviation from parallelism.

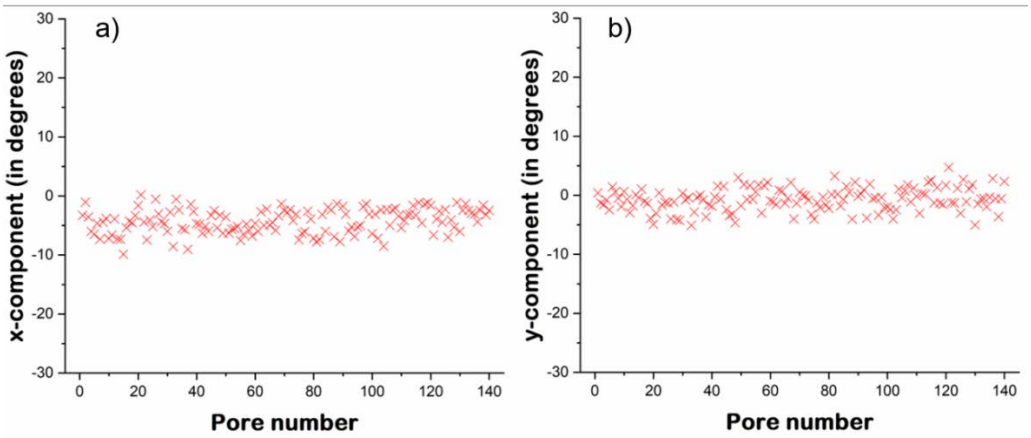

Figure 4. Regression analysis of the directions of all processed pores from the X-ray CT tomogram, **a)** showing the variation in the *x*-component **b)** showing the variation in the *y*-component. All values are in degrees and relative to the *z*-axis after initial coarse alignment of the volume.

The slight pore misalignment is attributed to the curvature of the solidification front during melting and is inherent to the LFZ technique. The macroscopic solid-liquid interface is frequently concave towards the melt [29], and the alignment of the eutectic grains proceeds perpendicular to this interface so that some deviation of the fibre direction from the axis of the solidified rod is commonly encountered. For typical support diameters and thicknesses above ~1 mm, misalignment may result in a significant reduction of the proportion of pores percolating between both sides of the membrane. Therefore, supports that are as thin as possible are desirable.

4.2. Total electrical conductivity of an infiltrated rod

According to Equation 3, conductivity of both the solid and molten carbonate phases impact performance. Therefore, Figure 5 shows the total electrical conductivity of the ternary eutectic carbonate mixture (in an Al_2O_3 support) (red circles), carbonate-infiltrated MgSZ rod (blue triangles) and MgSZ-MgO eutectic sample (green squares), obtained from impedance spectroscopy measurements up to 460 °C (for the carbonate mixture), 600 °C (for carbonate infiltrated MgSZ) or 850 °C (for MgSZ-MgO eutectic).

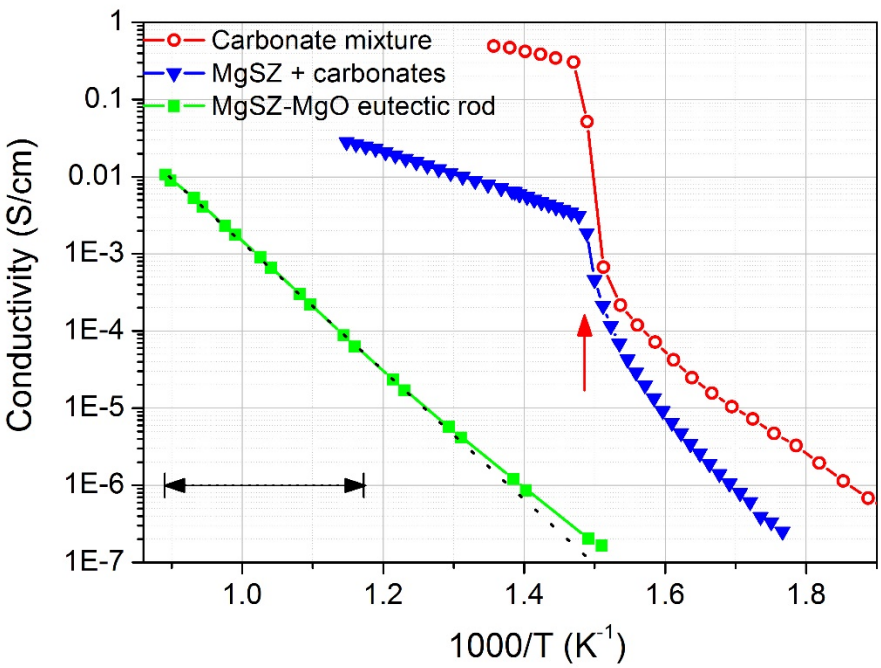

Figure 5. Total electrical conductivity of the eutectic mixture of carbonates (red circles), MgSZ porous matrix infiltrated with carbonates (blue triangles) and MgSZ-MgO as-grown eutectic (green squares). The dotted line is calculated with the parameters obtained from the fit of the expression $\sigma T = A\exp(-E_a/kT)$ to the experimental data of the MgSZ-MgO sample in the temperature range 580 °C to 850 °C (indicated with black arrowed-segment). The melting temperature of the carbonates (~400 °C) is marked with a red arrow.

The conductivity observed for the MgSZ-MgO eutectic is identical to the one reported in [38]. The activation energy for σT in the high temperature end (fit using data between 580 °C and 850 °C) was 1.73±0.01 eV. Regarding the samples infiltrated with carbonates, in both cases the conductivity increased at the carbonate melting temperature (~400 °C), as expected [46], but the conductivity above this temperature is 65 times larger for the molten carbonates than for the MgSZ-carbonate infiltrated sample. This may be due to the combined effect of several factors: the most evident one is that the pore proportion is at most 29% vol, according to the ZrO_2-MgO PD, further limited to ~22.4 to 27% because of incomplete etching. Other factors come from pores not percolating between both sides of the support, either because they are half-closed or because they end at the rod side surfaces instead of at its bases where the electrodes are attached. The latter aspect arises from pore misalignment, as found by X-ray nano-CT, and may be significant at the ≥2 mm length of the sample used in conductivity experiment. As explained above, some misalignment is unavoidable in LFZ processed materials, owing to the curvature of the solidification front. In any case, from Figure 5, the total electrical conductivity *via* the molten carbonate path is still much larger than the conductivity of oxide ions *via* the MgSZ oxide phase in the temperature range of interest, as expected for the combination of a solid oxide and a molten salt typical of supported molten-salt membranes.

5. Membrane assembly and permeation experiments

As-grown rods were ~1.5 mm diameter and ~80 mm long. Each rod was cut into ~2 mm-long slices that were acid-etched for ≥20 days to dissolve the MgO fibres. To increase the effective membrane surface area, seven MgSZ porous slices were inserted into circular holes (~1.6 mm diameter) which were laser-drilled in a 500 µm-thick YSZ ceramic plate. Ceramabond 885 was used to secure the rods within the plate (Figure 6).

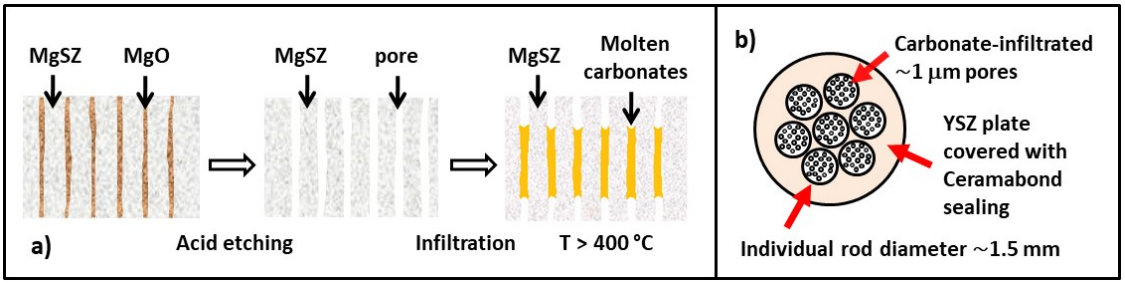

Figure 6. Schematics showing **a)** etching and infiltration steps applied to the as-grown MgSZ-MgO eutectic rods, and **b)** the arrangement of seven infiltrated transverse rod portions forming the membrane to be used in the permeation experiment. For the permeation experiments, carbonates were infiltrated after the seven etched rods were pasted to the support.

The membrane formed by the seven etched rods was pasted to a 11-mm-diameter, 250-mm-long YSZ tube. A pellet of pressed carbonate powders containing the quantity required to fully infiltrate the pores, was deposited on top of the support, then the tube was inserted into the membrane reactor, which was placed inside the furnace. The temperature was first increased from room temperature to 495 °C at 1 °C.min^{-1} under 30 ml.min^{-1} flow of composition 50%CO_2/25%N_2/25%O_2, both at the feed and permeate side inlets (this procedure ensures that the carbonates do not decompose during heating). The membrane was held for several hours at 495 °C to allow the carbonates to fully infiltrate the pores by capillarity. Then, the sweep gas was switched to 30 ml.min^{-1} of high-purity Ar (to generate a driving force for CO_2 permeation) and the temperature was increased first to 565 °C and then from 565 to 815 °C in steps of 50 °C, with 7 or 10 h of holding time at each temperature step and 1 °C.min^{-1} ramp between steps.

Figure 7 shows the temperature dependence of the CO_2 and O_2 fluxes, taking the sum of the seven rod sections (including solid plus molten phase) as the effective membrane area, A = 12 mm^2. Average flux values are determined after 7 or 10 h of dwell time at each temperature, except at 815 °C, as CO_2 permeation showed a steep decrease after only 1 h at that temperature (see Figure S5 in the ESI). This behaviour is discussed below. Since there is no obvious transport mechanism to enable significant N_2 permeation, the detection of a significant N_2 flux at the permeate-side outlet can be attributed to a leak. The N_2 flux in the present measurements was always around the background level of N_2 in the analytical instrumentation, so that we may safely consider that leaks are negligible in our membrane. Therefore, the CO_2 to N_2 selectivity across all temperatures was very high, as expected for supported molten-salt membranes [47]. The O_2 flux, on the contrary, is above the background level beyond 700 °C, implying that there is O_2 permeation through the membrane, discussed below.

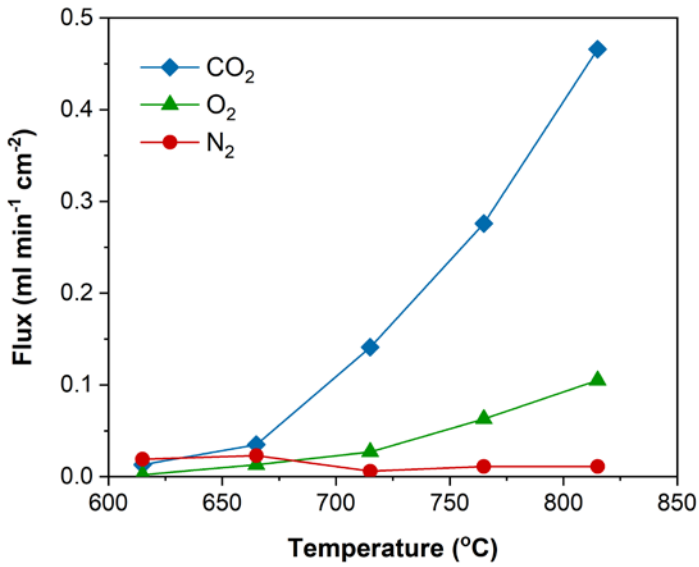

Figure 7. CO_2, O_2 and N_2 fluxes obtained in the permeation experiment of the carbonate-infiltrated MgSZ membrane.

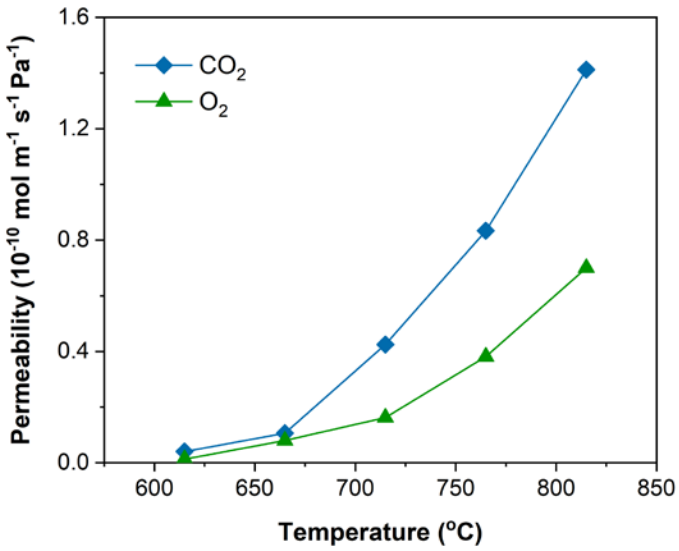

Figure 8. CO_2 and O_2 permeability of the carbonate-infiltrated MgSZ membrane.

Figure 8 shows the CO_2 (P_{CO2}) and O_2 (P_{O2}) permeabilities (in $mol.m^{-1}.s^{-1}.Pa^{-1}$) obtained from the corresponding flux through the expression $P= J.t/(p_i-p_o)$, where t is the membrane thickness (here, approximated by the length of the rods) and p_i, p_o are the CO_2 or O_2 partial pressures at the feed and permeate sides, respectively. The CO_2 permeability is 0.83×10^{-10} $mol.m^{-1}.s^{-1}.Pa^{-1}$ at 765 °C and 1.41×10^{-10} $mol.m^{-1}.s^{-1}.Pa^{-1}$ at 815 °C, much higher than in ceramic membranes based on YSZ as ionic conducting phase (10^{-11} $mol.m^{-1}.s^{-1}.Pa^{-1}$ at 850 °C in [4] and 7.69×10^{-13} $mol.m^{-1}.s^{-1}.Pa^{-1}$ at 650 °C in [48]), despite the lower conductivity of MgSZ compared

to YSZ, and of the same order as the best performing membranes reported to date using SDC supports and different types of pore-formers [14,16].

Figures 7 and 8 suggest that the permeation of both CO_2 and O_2 responds to a thermally activated mechanism. An Arrhenius fit of the permeability data yields activation energies of 1.5(2) and 1.3(1) eV for CO_2 and O_2, respectively, which are in reasonable agreement with the activation energy for the oxygen ion conduction of the MgSZ matrix determined in Section 4 and in previous reports ($E_a(\sigma_{so}T)$= 1.73(1) eV) [38].

The steep decrease of the permeation flux after 1 h at 815 °C (Figure S5, ESI) is intriguing. It cannot be attributed to a leak or breaking of the membrane, because that would likely result in an increase in CO_2 flux, contrary to observation. To understand that behaviour we analysed by Raman spectroscopy and XRD the evolution of an infiltrated sample submitted to a similar thermal treatment as the membrane (reaching 800 °C). The Raman spectra shown in Figure S6 of the ESI shows that after the treatment the matrix has evolved from the initial cubic-fluorite phase to a superposition of cubic, tetragonal and monoclinic phases of ZrO_2, with undetermined Mg content, a behaviour that is attributed to phase segregation. In fact, as the PD of the ZrO_2-MgO shows (Figure S1, ESI), the cubic phase of MgSZ is not stable below 1400 °C and segregation between tetragonal or monoclinic MgO-poor ZrO_2 and MgO phases is expected in that temperature range, as previously reported [49]. MgO is Raman-inactive, so that the presence of this phase cannot be detected by this technique. XRD of the same sample, shown in Figure S7, further showed the presence of a fluorite-like phase with a lattice parameter suggesting a cation composition close to that of the metastable $Mg_2Zr_5O_{12}$ phase [50]. Segregation, however, requires annealing times of the order of 24 h at 1200 °C in bulk MgSZ (Figure S8) [49], such that it is surprising that it occurs in just 1 h at 815 °C during the permeation experiment. We have found that the fast segregation is a consequence of the porous character of the sample used to fabricate the membrane: the same treatment in a non-etched sample did not affect the MgSZ structure whereas segregation was seen after just 1 h at 800 °C in an etched, non-infiltrated sample. The support instability above 800 °C limits its applicability at such high temperatures. On the other hand, the membrane was held for 10 h at 765 °C with no hint of failure or decreasing performance, so we can assume that 765 °C is still a safe operating temperature.

The behaviour of an infiltrated MgSZ support at high temperature was further investigated to elucidate the possible formation of alkali-metal zirconates through reactions such as $ZrO_2 + Li_2CO_3 \rightleftarrows Li_2ZrO_3 + CO_2$, as observed in [8]. Although no hint of either m- or t-Li_2ZrO_3 was found by Raman spectroscopy, a weak peak was detected at 23.3° in the XRD pattern shown in

Figure S7 that cannot be assigned to any of the already mentioned phases and is close to the main peak of t-Li_2ZrO_3, expected at 23.1°. The intensity of the peak at ~23° is close to the detection limit of X-ray diffraction but its likely attribution to Li_2ZrO_3 suggests that the appearance of this phase has to be considered when dealing with zirconia-derived phases.

6. Discussion

We note that the measured CO_2 permeability is much higher than those reported for YSZ-based supported molten-salt membranes [4,48], despite the conductivity of MgSZ being approximately one order of magnitude lower than that of YSZ. The high permeability therefore may be attributed to the improved pore characteristics: good connectivity, alignment along the permeation direction, very homogeneous pore size and high specific surface. The ordered pore distribution also reduces the ceramic support tortuosity factor.

To take advantage of the high permeability observed in the present material, bigger samples are needed. Other available solidification methods that allow larger ingots may be used [51,32]. Alternatively, a more cost-effective approach could be to coat the surface of an appropriately designed ceramic (either tube or plate) with the solidified eutectic coating [52,53].

The high CO_2 flux reported in Figure 7 warrants some discussion. Experimental values can be compared with predicted ones by substituting in Equations 2 and 3 the appropriate values of CO_2 partial pressures, membrane thickness and carbonate and MgSZ conductivities. For the solid oxide phase [$(\varphi/\tau)_{so}\sigma_{so}$], we use the conductivity of the MgSZ-MgO eutectic (see Figure 5), since MgO is non-conducting and the eutectic presents, *a priori*, the same volume fraction and tortuosity factor as the matrix used for the membrane. For the carbonate phase, we take the conductivity of the molten carbonates reported in Figure 5 and, to compare with the best possible situation, assume an optimal microstructure in which all the pores are perfectly aligned and contribute to permeation, i.e. $(\varphi/\tau)_c$ = 0.29/1. The actual value will be lower, but this will not be relevant since the total conductivity will be limited by that of the solid oxide. With these assumptions the CO_2 flux expected at 800 °C would be ~1.8 x 10^{-2} ml.min^{-1}.cm^{-1}, which is ~25 times lower than the observed value.

To explain this discrepancy, we first consider the possibility of σ_{so} being higher in the membrane than in the as-grown eutectic. As explained in Section 4, the Mg cation content of the MgSZ matrix found by EDS analysis (17%) is below that predicted by the ZrO_2-MgO PD (~20%), a difference that has been attributed to the leaching effect of the acid treatment. Since the

conductivity of $Zr_{1-x}Mg_xO_{2-x}$ presents a maximum around x= 0.08-0.09 [54,55], the observed reduction of the Mg content after leaching might enhance the conductivity. The reduction in Mg content, however, is too low to account for the increase of σ_{eff} that would be required to explain the high flux.

We then must consider an enhancement of the CO_2 flux related to the presence of O_2 in the feed gas (pO_2= 0.25 atm), an experimental condition not typically investigated for nominally oxygen-ion conducting supports. According to [5], both the CO_2 flux through the molten carbonates and the O_2 flux through the solid oxide phase might be enhanced in the presence of O_2 if the solid oxide were a mixed ionic-electronic conductor. Although there are no reports in the literature about *p*-type conductivity of MgSZ at high oxygen activities, we may take data from Y_2O_3 doped ZrO_2 (YSZ or TZP) as a reference, where the hole conductivities at 1 atm and ~700 °C are between 5 x 10^{-7} and 3 x 10^{-6} S.cm^{-1}. Looking at the expression for the CO_2 flux given in [5], we can say that with the likely very low hole conductivity of MgSZ, the expected increase of the CO_2 flux derived from the presence of O_2 would be very low. Similarly, the O_2 flux through the solid oxide would be much smaller than observed.

We must then conclude that the mechanism based on expressions (1) and (2) are insufficient to describe the CO_2 and O_2 flux results. As formulated, the model assumes bulk diffusion by carbonate and oxygen ions through the molten salt and solid support, respectively, but does not account for specific microstructural details such as the length of the triple-phase-boundaries (TPB) where Equation 1 takes place. Moreover, assuming Equation 1 is the only mechanism taking place omits the possible contribution of other mechanisms involving reactions at the support-salt interfaces. One example is CO_2 transport mediated by pyrocarbonate $C_2O_5^{2-}$ ions [56], formed through the surface Reaction 4:

$$CO_{2(g)} + CO_3^{2-}{}_{(l)} \rightleftarrows C_2O_5^{2-}{}_{(l)}, \quad (4)$$

together with the interfacial Reaction 5:

$$C_2O_5^{2-}{}_{(l)} + O^{2-}{}_{(so)} \rightarrow 2CO_3^{2-}{}_{(l)}. \quad (5)$$

A combination of reactions (1), (4) and (5) might explain the permeation and, at the same time, account for the likely involvement of the solid oxide ionic conduction. Although at this stage this conclusion is not more than a hypothesis, it is supported by the distinctive characteristics of the MgSZ support used here: besides the reduced tortuosity factor arising from almost parallel pore alignment, the high pore density and their micrometric size provides a high specific length of TPB at the membrane surfaces and also a high volume-specific interfacial area between the

support and the molten phase for reactions (1) and (5) to take place. More experiments are foreseen to validate this hypothesis. Varying the growth rate during the directional solidification, for instance, would allow control of the pore diameter (and accordingly the internal surface area and TPB length) while maintaining the total pore fraction.

The detection of O_2 permeation does not have a simple explanation. O_2 permeation through the solid oxide in the form of O^{2-} ions requires the presence of electronic conductivity in either the oxide itself [5] or in the molten-carbonate phase [57]. Both possibilities do not seem likely, however; the electronic conductivity in MgSZ is expected to be negligible and, with regards to electronic conduction in the carbonate phase, this is still a proposition that has not been verified. The alternative is that oxygen permeates through the molten-carbonate phase in the form of CO_4^{2-} or CO_5^{2-}. This possibility has been proposed to explain the anomalously high O_2 flux in a metal-carbonate membrane [18] and is supported by DFT studies of different permeation mechanisms [21]. However, the proximity of the CO_2 to O_2 permeability ratio to 2:1 strongly points to both fluxes being related. The use of O_2 together with CO_2 in the feed gas for purely ionic conducting supports is uncommon but has been studied in membranes employing a mixed ionic-electronic conductor as the supporting matrix [5]. In [58], it was shown that CO_2 and O_2 permeation were interlinked so that in the absence of CO_2 there was no measurable O_2 permeation. In another work [59], using an SDC support and 15% CO_2, 10% O_2 in the feed gas, both CO_2 and O_2 gases were found at the permeate side and the CO_2 flux was enhanced as pO_2 was increased, but the authors attributed the occurrence of O_2 permeation to the mixed ionic-electronic conducting character of SDC. More experimental work is clearly needed to elucidate the complex permeation mechanisms taking place in this type of membrane.

7. Summary and Conclusions

We have successfully produced a supported molten-salt membrane using a porous matrix, obtained by acid-etching a fibrilar MgSZ-MgO eutectic, as a ceramic support. The parent material was obtained by a laser-assisted directional solidification, demonstrating a new method for the preparation of laboratory-scale membranes with highly aligned pores which percolate between feed and permeate sides. This preparation method is applicable to a range of oxide materials, which will be useful for probing geometrical and mechanistic aspects of membrane permeation in the future. Here we have demonstrated that the supports confer a high permeability value of 1.41×10^{-10} $mol.m^{-1}.s^{-1}.Pa^{-1}$ at 815 °C, which was attributed to the excellent pore and solid-oxide microstructural characteristics: good pore connectivity and alignment, high pore specific density

and homogeneous micrometric pore size. These properties are specific to the directional-solidification preparation process and add to the properties common to supported molten-salt membranes, such as suitability for high-temperature operation and very high CO_2/N_2 selectivity. The good performance of the membrane reported here supports future efforts, both in experimentation and modelling, to understand the mechanisms involved in this type of membrane.

Acknowledgments

The authors acknowledge the financial support from the Spanish Ministerio de Economía y Competitividad and Feder Funds under project MAT2016-77769R. L. Grima acknowledges financial support through grant BES-2017-079683 associated to the aforementioned project. The research leading to these results has received funding from the European Research Council under the European Union's Seventh Framework Programme (FP/2007-2013)/ERC Grant Agreement Number 320725 and from the Engineering & Physical Sciences Research Council (EPSRC) *via* grants EP/M01486X/1, EP/P007767/1 and EP/P009050/1. PRS acknowledges the Royal Academy of Engineering (CiET1718/59). PRS, DJLB, JJB and MDK acknowledge the support of The Faraday Institution (faraday.ac.uk; EP/ S003053/1). G. Mutch was supported by the Royal Academy of Engineering under the Research Fellowship Scheme and would like to thank the EPSRC for his Doctoral Prize Fellowship (EP/M50791X/1) and Newcastle University for a Newcastle University Academic Track (NUAcT) Fellowship. X-Ray CT acquisition and analysis was supported by UCL and EPSRC under EP/N032888/1. We thank the Servicio General de Apoyo a la Investigación-SAI (Universidad de Zaragoza) for technical support in X-ray diffraction and electron microscopy experiments, Rubén Gotor for technical assistance in sample preparation and R. Lahoz for laser-drilling the YSZ plate that serves as the membrane base. Data supporting this publication is available under a Creative Commons Attribution 4.0 International license, see DOI: 10.25405/data.ncl.13019249.

References

[1] H.B. Park, J. Kamcev, L.M. Robeson, M. Elimelech, B.D. Freeman, Maximizing the right stuff: The trade-off between membrane permeability and selectivity, Science 356 (2017) 1138–1148.

[2] G.A. Mutch, L. Qu, G. Triantafyllou, W. Xing, M.-L. Fontaine, I.S. Metcalfe, Supported molten-salt membranes for carbon dioxide permeation, J. Mater. Chem. A7 (2019) 12951–12973.

[3] P. Zhang, J. Tong , K. Huang, X. Zhu, W. Yang, The current status of high temperature electrochemistry-based CO_2 transport membranes and reactors for direct CO_2 capture and conversion, Progress in Energy and Combustion Science 82 (2021) 100888.

[4] J.L. Wade, K.S. Lackner, A.C. West, Transport model for a high temperature, mixed conducting CO_2 separation membrane, Solid State Ionics 178 (2007) 1530–1540.
[5] Z. Rui, M. Anderson, Y.S. Lin, Y. Li, Modeling and analysis of carbon dioxide permeation through ceramic-carbonate dual-phase membranes, J. Membr. Sci. 345 (2009) 110–118.
[6] Y. Li, Z. Rui, C. Xia, M. Anderson, Y.S. Lin, Performance of ionic-conducting ceramic/carbonate composite material as solid oxide fuel cell electrolyte and CO_2 permeation membrane, Catalysis Today 148 (2009) 303–309.
[7] M. Anderson, Y.S. Lin, Carbonate–ceramic dual-phase membrane for carbon dioxide separation, J. Membr. Sci. 357 (2010) 122–129.
[8] J.L. Wade, C. Lee, A.C. West, K.S. Lackner, Composite electrolyte membranes for high temperature CO_2 separation, J. Membr. Sci. 369 (2011) 20–29.
[9] J. Ortiz-Landeros, T. Norton, Y.S. Lin, Effects of support pore structure on carbon dioxide permeation of ceramic-carbonate dual-phase membranes, Chem. Eng. Sci. 104 (2013) 891–898.
[10] T.T. Norton, Y.S. Lin, Ceramic-carbonate dual-phase membrane with improved chemical stability for carbon dioxide separation at high temperature, Solid State Ionics 263 (2014) 172–179.
[11] X. Dong, J. Ortiz Landeros, Y.S. Lin, An asymmetric tubular ceramic-carbonate dual phase membrane for high temperature CO_2 separation, Chem. Commun. 49 (2013) 9654–9656.
[12] X. Dong, H.C. Wu, Y.S. Lin, CO_2 permeation through asymmetric thin tubular ceramic-carbonate dual-phase membranes, J. Membr. Sci. 564 (2018) 73–81.
[13] M. Zuo, S.J. Zhuang, X.Y. Tan, B. Meng, N.T. Yang, S.M. Liu, Ionic conducting ceramic-carbonate dual phase hollow fibre membranes for high temperature carbon dioxide separation, J. Membr. Sci. 458 (2014) 58–65.
[14] T. Chen, Z. Wang, J. Hu, M.H. Wai, S. Kawi, Y.S. Lin, High CO_2 permeability of ceramic-carbonate dual-phase hollow fiber membrane at medium-high temperature, J. Membr. Sci. 597 (2020) artn 117770.
[15] Y. Shilong, Y. Zhupeng, L. Chuanming, C. Xiaowei, Z. Yanwei, Theoretical description on the interface-enhanced conductivity of SDC/LiNa-carbonate composite electrolytes, Mater. Lett. 92 (2013) 78–81.
[16] L. Zhang, N. Xu, X. Li, S. Wang, K. Huang, W. H. Harris, W. K. S. Chiu, High CO_2 permeation flux enabled by highly interconnected three dimensional ionic channels in selective CO_2 separation membranes, Energy Environ. Sci. (2012) 5, 8310–8317.
[17] M. Kazakli, G.A. Mutch, G. Triantafyllou, A.G. Gil, T. Li, B. Wang, J.J. Bailey, D.J.L. Brett, P.R. Shearing, K. Li, I. Metcalfe, Controlling molten carbonate distribution in dual-phase molten salt-ceramic membranes to increase carbon dioxide permeation rates, J. Membr. Sci. 617 (2021) 118640.
[18] J. Fang, J. Tong, K. Huang, A superior mixed electron and carbonate-ion conducting metal-carbonate composite membrane for advanced flue-gas carbon capture, J. Membr. Sci. 505 (2016) 225–230.
[19] J. Fang, N. Xu, T. Yang, P. Zhang, J. Tong, K. Huang, CO_2 capture performance of silver-carbonate membrane with electrochemically dealloyed porous silver matrix, J. Membr. Sci. 523 (2017) 439–445.
[20] L. Zhang, Y. Gong, K.S. Brinkman, T. Wei, S. Wang, K. Huang, Flux of silver-carbonate membranes for post-combustion CO_2 capture: The effects of membrane thickness, gas concentration and time, J. Membr. Sci. 455 (2014) 162–167.
[21] L. Zhang, J. Tong, Y. Gong, M. Han, S. Wang, K. Huang, Fast electrochemical CO_2 transport through a dense metal-carbonate membrane: A new mechanistic insight, J. Membr. Sci. 468 (2014) 373–379.
[22] H. Huang, S. Cheng, J. Gao, C. Chen, J. Yi, Phase-inversion tape-casting preparation and significant performance enhancement of $Ce_{0.9}Gd_{0.1}O_{1.95}$–$La_{0.6}Sr_{0.4}Co_{0.2}Fe_{0.8}O_{3-\delta}$ dual-phase asymmetric membrane for oxygen separation, Mater. Lett. 137 (2014) 245–248.
[23] C. Gaudillere, J.M. Serra, Freeze-casting: Fabrication of highly porous and hierarchical ceramic supports for energy applications, Bol. Soc. Esp. Ceram. Vidr. 55 (2016) 45–55.
[24] A.R. Studart, U.T. Gonzenbach, E.L. Tervoort, J. Gauckler, Processing Routes to Macroporous Ceramics: A Review, J. Amer. Ceram. Soc. 89 (2006) 1771–1789.
[25] B.F.K. Kingsbury, K. Li, A morphological study of ceramic hollow fibre membranes, J. Membr. Sci. 328 (2009) 134–140.

[26] W.Y. Choi, H.E. Kim, Y.W. Moon, K.H. Shin, Y.H. Koh, Production of porous Calcium Phosphate Ceramics with Aligned Pores using Ceramic/Camphene-based co-extrusion, Biomaterials Research 19 (2015) 16 (7 pages).
[27] L.A. McNeil, G.A. Mutch, F. Iacoviello, J.J. Bailey, G. Triantafyllou, D. Neagu, T.S. Miller, E.I. Papaioannou, W. Hu, D.J.L. Brett, P.R. Shearing, I.S. Metcalfe, Dendritic silver self-assembly in molten-carbonate membranes for efficient carbon dioxide capture, Energy Environ. Sci. 13 (2020) 1766-1775.
[28] P. Rudolph, T. Fukuda, Fiber Crystal Growth from the Melt. Cryst. Res. Technol. 34 (1999) 3–40.
[29] J. Llorca, V.M. Orera, Directionally solidified eutectic ceramic oxides, Progress in Materials Science 51 (2006) 711–809.
[30] Phase Equilibria Diagrams Online Database (NIST Standard Reference Database 31), The American Ceramic Society and the National Institute of Standards and Technology, 2020, Figure Number Zr-076-A.
[31] J. Echigoya, H. Suto, S. Hayashi, Growth Morphology and Orientation Relationships in Directionally Solidified MgO-ZrO_2 Eutectic, Transactions of the Japan Institute of Metals 26 (1985) 895–900.
[32] F.L. Kennard, R.C. Bradt, V.S. Stubican, Directional solidification of ZrO_2-MgO eutectic, J. Amer. Ceram. Soc. 57 (1974) 428–431.
[33] G. Fiquet, P. Richet, G. Montagnac, High-temperature thermal expansion of lime, periclase, corundum and spinel, PhysChem Minerals 27 (1999) 103–111.
[34] Y. Shiratori, F. Tietz, H.P. Buchkremer, D. Stöver, YSZ–MgO composite electrolyte with adjusted thermal expansion coefficient to other SOFC components, Solid State Ionics 164 (2003) 27–33.
[35] V.M. Orera, R.I. Merino, J.A. Pardo, A. Larrea, J.I. Peña, C. González, P. Poza, J.Y. Pastor, J. LLorca, Microstructure and physical properties of some oxide eutectic composites processed by directional solidification, Acta Mater. 48 (2000) 4683–4689.
[36] D. Sola, P.B. Oliete, R.I. Merino, J.I. Peña, Directionally solidified Ni doped MgO-MgSZ eutectic composites for thermophotovoltaic devices, J. Eur. Ceram. Soc. 39 (2019) 1206–1213.
[37] S.P.S. Badwal, Zirconia-based solid electrolytes: microstructure, stability and ionic conductivity, Solid State Ionics 52 (1992) 23-32.
[38] R.I. Merino, V.M. Orera, J.I. Peña, G.F. de la Fuente, Conductivity anisotropy in directionally solidified $CaZrO_3$-CaSZ and MgO-MgSZ eutectics, Solid State Ionics 100 (1997) 313–318.
[39] J.J. Bailey, T.M.M. Heenan, D.P. Finegan, X. Lu, S.R. Daemi, F. Iacoviello, N.R. Backeberg, O.O. Taiwo, D.J.L. Brett, A. Atkinson, P.R. Shearing, Laser-preparation of geometrically optimised samples for X-ray nano-CT, J. Microscopy 267 (2017) 384–396.
[40] C. Sommer, C. Straehle, U. Köthe, F.A. Hamprecht, Ilastik: Interactive learning and segmentation toolkit, IEEE International Symposium on Biomedical Imaging: From Nano to Macro, Chicago, IL, 2011, pp. 230-233, doi: 10.1109/ISBI.2011.5872394.
[41] Impedance Spectroscopy: Theory, Experiments and Applications, E. Barsoukov, J. R. Macdonald (Eds.), Wiley-Interscience, Hoboken, 2005.
[42] S.G. Patrício, E.I. Papaioannou, B.M. Ray, I.S. Metcalfe, F.M.B. Marques, Composite CO_2 separation membranes: Insights on kinetics and stability, J. Membr. Sci. 541 (2017) 253–261.
[43] K.A. Jackson, J.D. Hunt, Lamellar and rod eutectic growth. Transactions of the Metallurgical Society of AIME 236 (1966) 1129–1142.
[44] T. Sato, T. Endo, M. Shimada, T. Mitsudome, N. Otabe, Hydrothermal corrosion of Mg-partially stabilized zirconia, J. Mat. Sci. 26 (1991) 1346–1350.
[45] M. Yashima, N. Ishizawa, N., M. Yoshimura, Application of an Ion-Packing Model Based on Defect Clusters to Zirconia Solid Solutions: II, Applicability of Vegard's law, J. Amer. Ceram. Soc. 75 (1992) 1550–1557.
[46] H. Näfe, Conductivity of Alkali Carbonates, Carbonate-Based Composite Electrolytes and IT-SOFC, ECS J. Solid State Science and Technology 3 (2014) N7–N14.
[47] M.R. Cerón, L.S. Lai, S. Amiri, M. Monte, S. Katta, J.C. Kelly, M.A. Worsley, M.D. Merrill, S. Kim, P.G. Campbell, Surpassing the conventional limitations of CO_2 separation membranes with hydroxide/ceramic dual-phase membranes, J. Membr. Sci. 567 (2018) 191–198.
[48] B. Lu, Y.S. Lin, Synthesis and characterization of thin ceramic-carbonate dual-phase membranes for carbon dioxide separation, J. Membr. Sci. 444 (2013) 402–411.
[49] J. Echigoya, K. Sasai, H. Suto, Decomposition of cubic ZrO_2 in MgO-ZrO_2 eutectic, Transactions of The Japan Institute of Metals 27 (1986) 247–253.

[50] S.C. Farmer, L.H. Schoenlein, A.H. Heuer, Precipitation of $Mg_2Zr_5O_{12}$ in MgO-Partially-Stabilized ZrO_2, J. Am. Ceram. Soc. 66 (1983) c-107–c-109.
[51] N. Nakagawa, H. Ohtsubo, A. Mitani, K. Shimizu, Y. Waku, High temperature strength and thermal stability for melt growth composite, J. Eur. Ceram. Soc. 25 (2005) 1251–1257.
[52] J. Gurauskis, V. Lennikov, G.F. de la Fuente, R.I. Merino, Laser-assisted, crack-free surface melting of large eutectic ceramic bodies, J. Eur. Ceram. Soc. 31 (2011) 1251–1256.
[53] R. Campana, A. Larrea, J.I. Peña, V.M. Orera, J. Eur. Ceram. Soc. 29 (2009) 85–90.
[54] T. Wen, L. Xiaofei, K. Chukun, W. Weppner, Conductivity of MgO-doped ZrO_2, Solid State Ionics 18&19 (1986) 715–719.
[55] W. Deng, Y. Li, High-temperature electrical properties of polycrystalline MgO-doped ZrO_2, Mat. Res. Bull. 113 (2019) 182–189.
[56] L. Zhang, X. Huang, C. Qin, K. Brinkman, Y. Gong, S. Wang, K. Huang, First spectroscopic identification of pyrocarbonate for high CO_2 flux membranes containing highly interconnected three dimensional ionic channels, Phys. Chem. Chem. Phys. 15 (2013) 13147–13152.
[57] H. Näfe, Electrochemical CO_2 Separation through an Alkali-Carbonate-Based Membrane, ECS J. Solid State Science and Technology 3 (2014) N23–N29.
[58] E.I. Papaioannou, H.Qi, I.S. Metcalfe, 'Uphill' permeation of carbon dioxide across a composite molten salt-ceramic membrane, J. Membr. Sci. 485 (2015) 87–93.
[59] J. Tong, L. Zhang, M. Han, K. Huang, Electrochemical separation of CO_2 from a simulated flue gas with high-temperature ceramic–carbonate membrane: New observations, J. Membr. Sci. 477 (2015) 1–6.